A numerical study of compact approximations based on flat integrated radial basis functions for second-order differential equations

C.M.T. Tien, N. Mai-Duy, C.-D. Tran, T. Tran-Cong*

Computational Engineering and Science Research Centre, Faculty of Health, Engineering and Sciences, The University of Southern Queensland, 487/521-535 West Street, Toowoomba, Queensland 4350, Australia.

Abstract

In this paper, we propose a simple but effective preconditioning technique to improve the numerical stability of Integrated Radial Basis Function (IRBF) methods. The proposed preconditioner is simply the inverse of a well-conditioned matrix that is constructed using non-flat IRBFs. Much larger values of the free shape parameter of IRBFs can thus be employed and better accuracy for smooth solution problems can be achieved. Furthermore, to improve the accuracy of local IRBF methods, we propose a new stencil, namely Combined Compact IRBF (CCIRBF), in which (i) the starting point is the fourth-order derivative; and (ii) nodal values of first- and second-order derivatives at side nodes of the stencil are included in the computation of first- and second-order derivatives at the middle node in a natural way. The proposed stencil can be employed in uniform/nonuniform Cartesian grids. The preconditioning technique in combination with the CCIRBF scheme employed with large values of the shape parameter are tested with elliptic equations and then applied to simulate several fluid flow problems governed by Poisson, Burgers, convection-diffusion, and Navier-Stokes equations. Highly accurate and stable solutions are obtained. In some cases, the preconditioned schemes are shown to be several orders of magnitude more accurate than those without preconditioning.

Keywords: RBF, Integrated RBF, Shape parameter, Ill-conditioning, ODE, PDE

---

*Corresponding author

Email addresses: camminhtri.tien@usq.edu.au (C.M.T. Tien), nam.mai-duy@usq.edu.au (N. Mai-Duy), canh-dung.tran@usq.edu.au (C.-D. Tran), thanh.tran-cong@usq.edu.au (T. Tran-Cong)

1. Introduction

During the last three decades, Radial Basis Function (RBFs) have found increasingly widespread use for numerical solution to the Partial Differential Equation (PDE) systems. Hardy [1, 2] devised Multi-Quadric (MQ) RBF schemes for scattered data fitting and general multi-dimensional data interpolation problems in geo-physical engineering. Buhmann [3] and Madych and Nelson [4] showed that MQ-RBF approximation methods converge exponentially as the density of RBFs and their shape parameters increase. Kansa first implemented MQ-RBFs (here referred to as Direct/Differential RBF or DRBF methods) for solving PDEs [5, 6]. Since then, DRBF methods have been increasingly used for the solution of elliptic, parabolic and hyperbolic PDEs which govern many engineering problems. In [7, 8, 9, 10, 11], practitioners demonstrated that the elliptic PDE solutions using DRBFs converge much faster than those based on polynomial approximations. Mai-Duy and Tran-Cong proposed the idea of using Indirect/Integrated RBFs (IRBFs) for the solution of PDEs [12, 13]. Numerical results in [12, 13, 14, 15, 16, 17, 18, 19] showed that the integral approach is more accurate than the differential approach. In these works, the authors claimed that because the integration is a smoothing operation and the integrated basis functions are of higher orders, the integral approach has the ability to yield a faster converging solution. In DRBF and IRBF methods, the original unknowns are the RBF coefficients. However, like the Differential Quadrature (DQ) method, these unknowns can be expressed in terms of nodal values of the dependent variable and the calculation is then conducted in the physical space [15].

However, despite the success of RBF methods in many scientific and engineering applications, their accuracy is dependent on a user defined parameter, namely the RBF width or the shape parameter. In this work, it is denoted by β. Numerical experiments indicated that the optimal value of β depends on the function to be interpolated, the configuration of nodal points, the RBF type, and the machine precision [3, 4, 9, 20, 21, 22, 23]. The matrix condition of the RBF method grows exponentially with the RBF width. For many problems, e.g. those having smooth solutions, the optimal value of the RBF width is known to be normally large however the corresponding coefficient matrix becomes ill-conditioned. An on-going problem involving the use of RBFs is how to choose the optimal value or even a consistently "good" value of β, which has received a great deal of attention of many researchers. Rippa [21] presented a leave-one-out cross-validation scheme for optimising the shape parameter. For smooth functions, it was shown that without round-off error the highest accuracy for a given number of nodal points is regularly achieved when the RBFs become increasingly flat [8]. Theoretical and computational aspects of increasingly flat RBF interpolations were discussed in [24]. Fornberg and Wright [11] proposed the Contour-Padé algorithm which can stably compute the whole region of the shape parameter on the complex plane. Many different approaches to enhance the stability of DRBF methods have been proposed, for example [23, 25, 26, 27, 28, 29, 30, 31, 32] and their references therein. For

IRBF approaches, Sarra [16] studied the case of global flat IRBFs. It was observed that the even-order IRBFs are generally most accurate and most poorly conditioned for large values of the shape parameter β. Additionally, numerical results in [15, 16] showed that the use of higher-order IRBFs can lead to better accuracy. Further discussions about RBF can be found in [33, 34, 35] and references therein.

Motivated by the aforementioned works, this paper proposes (i) an easy-to-implement but effective preconditioning technique for Compact IRBF (CIRBF) schemes to alleviate ill-condition problems arising from using large values of β; and (ii) a Combined Compact IRBF (CCIRBF) approximation scheme using high-order IRBFs to enhance the solution accuracy, especially in the large value range of β. Unlike compact schemes previously proposed in [19, 36, 37, 38], a preconditioning technique is employed here. The present preconditioned CCIRBF scheme is able to stably compute second-order PDE problems with much larger values of β. We derive expressions for evaluation of first- and second-order derivative operators for solving PDE problems and demonstrate the stability and accuracy of the new scheme through various numerical experiments. It should be emphasised that a mesh-free property of RBFs allows lengths between nodes in the stencil to be different. It will be shown that a high level of accuracy is still achieved when CCIRBF stencils are applied to problems with curved boundaries. The strength of RBF methods lies in their ability to deal with scattered data. In the present work, this strength is exploited in the context of Cartesian grid discretisations. It is noted that creating a Cartesian grid is generally much more efficient than creating a finite-element mesh, particularly for domains of non-rectangular shapes. Unlike RBF-DQ methods, our proposed approximations are compact, which helps achieve a high level of accuracy (e.g. avoid the loss of information in the approximation near the curved boundary).

The structure of this paper is organised as follows. Section 2 numerically discusses the condition number of IRBFs over a wide range of β. To enhance the accuracy, a new approximation scheme, CCIRBF, is proposed in Section 3. Following this, a simple preconditioning technique is proposed in Section 4 to retain the accuracy of the CCIRBF when working in the large value range of β. Numerical examples in which the CCIRBF results are compared with some other solutions, where appropriate, are presented in Section 5. Finally, some concluding remarks are given in Section 6.

2. Numerical observations on condition numbers of IRBFs

Several IRBF approximation schemes were previously reported in [12, 19, 37, 38] and they are summarised here for convenience. In IRBF approaches, the MQ function is usually chosen as the basis function

$$G_i(x) = \sqrt{(x - c_i)^2 + a_i^2}, \tag{1}$$

where c_i and a_i are the centre and the width of the i-th MQ, respectively. On a stencil, the set of nodal points is taken to be the same as the set of MQ

3

centres. The MQ width is defined as $a_i = \beta h_i$, where β is a positive scalar (the shape parameter) and h_i is the distance between the i-th node and its closest neighbour.

For second-order PDEs, the integral approach normally starts with the decomposition of the second-order derivatives of a variable, u, into RBFs

$$\frac{d^2 u(\eta)}{d\eta^2} = \sum_{i=1}^{m} w_i G_i(\eta), \tag{2}$$

where $\{G_i(\eta)\}_{i=1}^{m}$ is the set of RBFs; and $\{w_i\}_{i=1}^{m}$ is the set of weights/coefficients to be found. Approximate representations for the first-order derivatives and the functions itself are then obtained through the integration processes

$$\frac{du(\eta)}{d\eta} = \sum_{i=1}^{m} w_i I_{1i}(\eta) + c_1, \tag{3}$$

$$u(\eta) = \sum_{i=1}^{m} w_i I_{2i}(\eta) + c_1 \eta + c_2, \tag{4}$$

where $I_{1i}(\eta) = \int G_i(\eta) d\eta$, $I_{2i}(\eta) = \int I_{1i}(\eta) d\eta$, and c_1 and c_2 are the constants of integration. If basis functions are further integrated, the similar notation will be used, e.g. $I_{3i}(\eta) = \int I_{2i}(\eta) d\eta$ and $I_{4i}(\eta) = \int I_{3i}(\eta) d\eta$. Their analytic forms up to fourth-order are given in Appendix.

In general, the starting point in the integration process can be different. The IRBF scheme is said to be of order k if the starting point is the kth-order derivative. In the literature, numerical examples of [16, 39] showed that the higher the order of the IRBF, the higher the matrix condition number will be. To illustrate this trend, Figure 1 shows a comparison of condition numbers among the IRBFs against the shape parameter β with a fixed number of grid points of 31 on a domain of [0, 1]. However, when the number of RBFs is reduced to 3 and larger values of β are used, as shown in Figure 2, the observation just mentioned is reversed. It can be seen that the conditions of $\mathbf{G}$ are the highest while those of $\mathbf{I}_4$ are the lowest. The higher the order of the IRBF, the smaller the matrix condition number will be. This is a very interesting behavior for which, unfortunately, a theoretical explanation cannot be offered at this stage. This can be seen as another advantage of using integrated RBFs over differentiated ones when local RBF methods are employed with large values of β. It is noted that global IRBFs, where all RBFs are employed (i.e. the observation in Figure 1), are fully populated and tend to be ill-conditioned as β increases while local IRBFs using 3 RBFs (i.e. the observation in Figure 2) have more relaxed condition numbers and can be well-behaved up to a certain large value of β. It is shown shortly that three-point stencils have the advantage that the approximation at the interior nodes near the boundary does not involve the nodal values outside the domain.
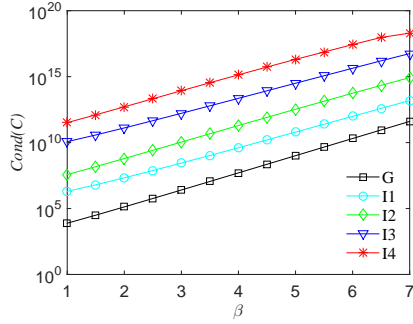
4

Figure 1: The effect of β on condition numbers of the IRBFs: the number of RBFs used is 31.
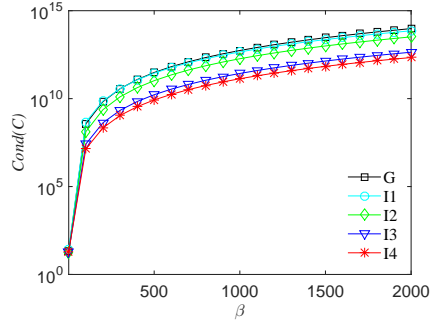
Figure 2: The effect of β on condition numbers of the IRBFs: the number of RBFs used is 3.

3. Combined compact integrated RBF scheme

From the above mentioned observations, we propose a new approximation method using the fourth-order derivative as the starting point in the process of integration in order to achieve better accuracy.

Consider a two-dimensional domain Ω, which is represented by a uniform Cartesian grid. The nodes are indexed in the x-direction by the subscript i ($i \in \{1, 2, ..., n_x\}$) and in the y-direction by j ($j \in \{1, 2, ..., n_y\}$). For rectangular domains, let N be the total number of nodes ($N = n_x \times n_y$) and N_{ip} be the number of interior nodes ($N_{ip} = (n_x - 2) \times (n_y - 2)$). At an interior grid point $\mathbf{x}_{i,j} = (x_{(i,j)}, y_{(i,j)})^T$ where $i \in \{2, 3, ..., n_x - 1\}$ and $j \in \{2, 3, ..., n_y - 1\}$, the associated stencils to be considered here are two local stencils: $\{x_{(i-1,j)}, x_{(i,j)}, x_{(i+1,j)}\}$ in the x-direction and $\{y_{(i,j-1)}, y_{(i,j)}, y_{(i,j+1)}\}$ in the y-direction. Hereafter, for brevity, η denotes either x or y in a generic local stencil $\{\eta_1, \eta_2, \eta_3\}$, where $\eta_1 < \eta_2 < \eta_3$ and $\eta_2 \equiv \eta_{(i,j)}$, are illustrated in Figure 3.
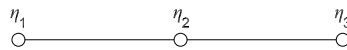

Figure 3: Compact three-point 1D-IRBF stencil for interior nodes.

The integral process of the present CCIRBF starts with the decomposition of fourth-order derivatives of a variable, u, into RBFs

$$\frac{d^4 u(\eta)}{d\eta^4} = \sum_{i=1}^{m} w_i G_i(\eta). \tag{5}$$

Approximate representations for the third- to first-order derivatives and the

5

functions itself are then obtained through the integration processes

$$\frac{d^3u(\eta)}{d\eta^3} = \sum_{i=1}^{m} w_i I_{1i}(\eta) + c_1, \tag{6}$$

$$\frac{d^2u(\eta)}{d\eta^2} = \sum_{i=1}^{m} w_i I_{2i}(\eta) + c_1\eta + c_2, \tag{7}$$

$$\frac{du(\eta)}{d\eta} = \sum_{i=1}^{m} w_i I_{3i}(\eta) + \frac{1}{2}c_1\eta^2 + c_2\eta + c_3, \tag{8}$$

$$u(\eta) = \sum_{i=1}^{m} w_i I_{4i}(\eta) + \frac{1}{6}c_1\eta^3 + \frac{1}{2}c_2\eta^2 + c_3\eta + c_4, \tag{9}$$

where $I_{1i}(\eta) = \int G_i(\eta)d\eta$, $I_{2i}(\eta) = \int I_{1i}(\eta)d\eta$, $I_{3i}(\eta) = \int I_{2i}(\eta)d\eta$, $I_{4i}(\eta) = \int I_{3i}(\eta)d\eta$, and c_1, c_2, c_3 and c_4 are the constants of integration. However, for the solution of second-order PDEs, only (7)-(9) are needed. It is noted that it is possible to implement integrated RBFs in higher dimensions to construct CIRBF. However, with the proposed compact approximation approach, the use of IRBFs in one dimension leads to conversion matrices of much smaller size and a relatively sparse system matrix.

150 *3.1. First-order derivative approximations*

For the combined compact approximation of the first-order derivatives at interior nodes, extra information is chosen as not only $\left\{\frac{du_1}{d\eta}; \frac{du_3}{d\eta}\right\}$ but also $\left\{\frac{d^2u_1}{d\eta^2}; \frac{d^2u_3}{d\eta^2}\right\}$. We construct the conversion system over a 3-point stencil as follows.

$$\begin{bmatrix} u_1 \\ u_2 \\ u_3 \\ \frac{du_1}{d\eta} \\ \frac{du_3}{d\eta} \\ \frac{d^2u_1}{d\eta^2} \\ \frac{d^2u_3}{d\eta^2} \end{bmatrix} = \underbrace{\begin{bmatrix} \mathbf{I}_4 \\ \mathbf{I}_3 \\ \mathbf{I}_2 \end{bmatrix}}_{\mathbf{C}} \begin{bmatrix} w_1 \\ w_2 \\ w_3 \\ c_1 \\ c_2 \\ c_3 \\ c_4 \end{bmatrix}, \tag{10}$$

155 where $\frac{du_i}{d\eta} = \frac{du}{d\eta}(\eta_i)$ with $i \in \{1,2,3\}$; $\mathbf{C}$ is the conversion matrix; and $\mathbf{I}_2$, $\mathbf{I}_3$, and $\mathbf{I}_4$ are defined as

$$\mathbf{I}_2 = \begin{bmatrix} I_{21}(\eta_1) & I_{22}(\eta_1) & I_{23}(\eta_1) & \eta_1 & 1 & 0 & 0 \\ I_{21}(\eta_3) & I_{22}(\eta_3) & I_{23}(\eta_3) & \eta_3 & 1 & 0 & 0 \end{bmatrix}. \tag{11}$$

$$\mathbf{I}_3 = \begin{bmatrix} I_{31}(\eta_1) & I_{32}(\eta_1) & I_{33}(\eta_1) & \frac{1}{2}\eta_1^2 & \eta_1 & 1 & 0 \\ I_{31}(\eta_3) & I_{32}(\eta_3) & I_{33}(\eta_3) & \frac{1}{2}\eta_3^2 & \eta_3 & 1 & 0 \end{bmatrix}. \tag{12}$$

6

$$\mathbf{I}_4 = \begin{bmatrix} I_{41}(\eta_1) & I_{42}(\eta_1) & I_{43}(\eta_1) & \frac{1}{6}\eta_1^3 & \frac{1}{2}\eta_1^2 & \eta_1 & 1 \\ I_{41}(\eta_2) & I_{42}(\eta_2) & I_{43}(\eta_2) & \frac{1}{6}\eta_2^3 & \frac{1}{2}\eta_2^2 & \eta_2 & 1 \\ I_{41}(\eta_3) & I_{42}(\eta_3) & I_{43}(\eta_3) & \frac{1}{6}\eta_3^3 & \frac{1}{2}\eta_3^2 & \eta_3 & 1 \end{bmatrix}. \tag{13}$$

Solving (10) yields

$$\begin{bmatrix} w_1 \\ w_2 \\ w_3 \\ c_1 \\ c_2 \\ c_3 \\ c_4 \end{bmatrix} = \mathbf{C}^{-1} \begin{bmatrix} u_1 \\ u_2 \\ u_3 \\ \frac{du_1}{d\eta} \\ \frac{du_3}{d\eta} \\ \frac{d^2u_1}{d\eta^2} \\ \frac{d^2u_3}{d\eta^2} \end{bmatrix}, \tag{14}$$

which maps the vector of nodal values of the function and its first- and second-order derivatives to the vector of RBF coefficients including the four integration constants. The first-order derivative at the middle point is computed by substituting (14) into (8) and taking $\eta = \eta_2$

$$\frac{du_2}{d\eta} = \underbrace{\mathbf{I}_{3m}\mathbf{C}^{-1}}_{\mathbf{D}_1} \begin{bmatrix} \mathbf{u} \\ \frac{du_1}{d\eta} \\ \frac{du_3}{d\eta} \\ \frac{d^2u_1}{d\eta^2} \\ \frac{d^2u_3}{d\eta^2} \end{bmatrix}, \tag{15}$$

or

$$\frac{du_2}{d\eta} = \mathbf{D}_1(1:3)\mathbf{u} + \mathbf{D}_1(4:5)\begin{bmatrix} \frac{du_1}{d\eta} \\ \frac{du_3}{d\eta} \end{bmatrix} + \mathbf{D}_1(6:7)\begin{bmatrix} \frac{d^2u_1}{d\eta^2} \\ \frac{d^2u_3}{d\eta^2} \end{bmatrix}, \tag{16}$$

where $\mathbf{D}_1$ is a row vector of length 7, the associated notation "$a:b$" is used to indicate the vector entries from the the column a to b; $\mathbf{u} = [u_1, u_2, u_3]^T$; and

$$\mathbf{I}_{3m} = \begin{bmatrix} I_{31}(\eta_2) & I_{32}(\eta_2) & I_{33}(\eta_2) & \frac{1}{2}\eta_2^2 & \eta_2 & 1 & 0 \end{bmatrix}. \tag{17}$$

By taking derivative terms to the left side and nodal variable values to the right side, (16) reduces to

$$\begin{bmatrix} -\mathbf{D}_1(4) & 1 & -\mathbf{D}_1(5) \end{bmatrix}\mathbf{u}' + \begin{bmatrix} -\mathbf{D}_1(6) & 0 & -\mathbf{D}_1(7) \end{bmatrix}\mathbf{u}'' = \mathbf{D}_1(1:3)\mathbf{u}, \tag{18}$$

where $\mathbf{u}' = \left[\frac{du_1}{d\eta}, \frac{du_2}{d\eta}, \frac{du_3}{d\eta}\right]^T$ and $\mathbf{u}'' = \left[\frac{d^2u_1}{d\eta^2}, \frac{d^2u_2}{d\eta^2}, \frac{d^2u_3}{d\eta^2}\right]^T$.

At the boundary nodes, the first-order derivatives are approximated in special compact stencils. Consider the boundary node η_1. Its associated stencil is $\{\eta_1, \eta_2, \eta_3, \eta_4\}$ as shown in Figure 4 and extra information is chosen as $\frac{du_2}{d\eta}$ and $\frac{d^2u_2}{d\eta^2}$.

Figure 4: Special compact four-point 1D-IRBF stencil for boundary nodes.

The conversion system over this special stencil is presented as the following matrix-vector multiplication

$$
\begin{bmatrix} u_1 \\ u_2 \\ u_3 \\ u_4 \\ \frac{du_2}{d\eta} \\ \frac{d^2 u_2}{d\eta^2} \end{bmatrix} = \underbrace{\begin{bmatrix} \mathbf{I}_{4sp} \\ \mathbf{I}_{3sp} \\ \mathbf{I}_{2sp} \end{bmatrix}}_{\mathbf{C}_{sp}} \begin{bmatrix} w_1 \\ w_2 \\ w_3 \\ w_4 \\ c_1 \\ c_2 \\ c_3 \\ c_4 \end{bmatrix},
\tag{19}
$$

where $\mathbf{C}_{sp}$ is the conversion matrix; and $\mathbf{I}_{2sp}$, $\mathbf{I}_{3sp}$, and $\mathbf{I}_{4sp}$ are defined as

$$
\mathbf{I}_{2sp} = \begin{bmatrix} I_{21}(\eta_2) & I_{22}(\eta_2) & I_{23}(\eta_2) & I_{24}(\eta_2) & \eta_2 & 1 & 0 & 0 \end{bmatrix}.
\tag{20}
$$

$$
\mathbf{I}_{3sp} = \begin{bmatrix} I_{31}(\eta_2) & I_{32}(\eta_2) & I_{33}(\eta_2) & I_{34}(\eta_2) & \frac{1}{2}\eta_2^2 & \eta_2 & 1 & 0 \end{bmatrix}.
\tag{21}
$$

$$
\mathbf{I}_{4sp} = \begin{bmatrix} I_{41}(\eta_1) & I_{42}(\eta_1) & I_{43}(\eta_1) & I_{44}(\eta_1) & \frac{1}{6}\eta_1^3 & \frac{1}{2}\eta_1^2 & \eta_1 & 1 \\ I_{41}(\eta_2) & I_{42}(\eta_2) & I_{43}(\eta_2) & I_{44}(\eta_2) & \frac{1}{6}\eta_2^3 & \frac{1}{2}\eta_2^2 & \eta_2 & 1 \\ I_{41}(\eta_3) & I_{42}(\eta_3) & I_{43}(\eta_3) & I_{44}(\eta_3) & \frac{1}{6}\eta_3^3 & \frac{1}{2}\eta_3^2 & \eta_3 & 1 \\ I_{41}(\eta_4) & I_{42}(\eta_4) & I_{43}(\eta_4) & I_{44}(\eta_4) & \frac{1}{6}\eta_4^3 & \frac{1}{2}\eta_4^2 & \eta_4 & 1 \end{bmatrix}.
\tag{22}
$$

Solving (19) yields

$$
\begin{bmatrix} w_1 \\ w_2 \\ w_3 \\ w_4 \\ c_1 \\ c_2 \\ c_3 \\ c_4 \end{bmatrix} = \mathbf{C}_{sp}^{-1} \begin{bmatrix} u_1 \\ u_2 \\ u_3 \\ u_4 \\ \frac{du_2}{d\eta} \\ \frac{d^2 u_2}{d\eta^2} \end{bmatrix}.
\tag{23}
$$

The boundary value of the first-order derivative of u is thus obtained by substituting (23) into (8) and taking $\eta = \eta_1$

$$
\frac{du_1}{d\eta} = \underbrace{\mathbf{I}_{3b}\mathbf{C}_{sp}^{-1}}_{\mathbf{D}_{1sp}} \begin{bmatrix} \mathbf{u} \\ \frac{du_2}{d\eta} \\ \frac{d^2 u_2}{d\eta^2} \end{bmatrix},
\tag{24}
$$

8

or

$$\frac{du_1}{d\eta} = \mathbf{D}_{1sp}(1:4)\mathbf{u} + \mathbf{D}_{1sp}(5)\frac{du_2}{d\eta} + \mathbf{D}_{1sp}(6)\frac{d^2u_2}{d\eta^2}, \qquad (25)$$

where $\mathbf{u} = [u_1, u_2, u_3, u_4]^T$ and

$$\mathbf{I}_{3b} = \begin{bmatrix} I_{31}(\eta_1) & I_{32}(\eta_1) & I_{33}(\eta_1) & I_{34}(\eta_1) & \frac{1}{2}\eta_1^2 & \eta_1 & 1 & 0 \end{bmatrix}. \qquad (26)$$

By taking derivative terms to the left side and nodal variable values to the right side, (25) reduces to

$$\begin{bmatrix} 1 & -\mathbf{D}_{1sp}(5) & 0 & 0 \end{bmatrix}\mathbf{u}' + \begin{bmatrix} 0 & -\mathbf{D}_{1sp}(6) & 0 & 0 \end{bmatrix}\mathbf{u}'' = \mathbf{D}_{1sp}(1:4)\mathbf{u}, \quad (27)$$

where $\mathbf{u}' = \left[\frac{du_1}{d\eta}, \frac{du_2}{d\eta}, \frac{du_3}{d\eta}, \frac{du_4}{d\eta}\right]^T$ and $\mathbf{u}'' = \left[\frac{d^2u_1}{d\eta^2}, \frac{d^2u_2}{d\eta^2}, \frac{d^2u_3}{d\eta^2}, \frac{d^2u_4}{d\eta^2}\right]^T$.

3.2. Second-order derivative approximations

For the combined compact approximation of the second-order derivatives at interior nodes, we employ the same extra information used in the approximation of the first-order derivative, involving $\left\{\frac{du_1}{d\eta}; \frac{du_3}{d\eta}\right\}$ and $\left\{\frac{d^2u_1}{d\eta^2}; \frac{d^2u_3}{d\eta^2}\right\}$. Therefore, the second-order derivative at the middle point is computed by simply substituting (14) into (7) and taking $\eta = \eta_2$

$$\frac{d^2u_2}{d\eta^2} = \underbrace{\mathbf{I}_{2m}\mathbf{C}^{-1}}_{\mathbf{D}_2}\begin{bmatrix} \mathbf{u} \\ \frac{du_1}{d\eta} \\ \frac{du_3}{d\eta} \\ \frac{d^2u_1}{d\eta^2} \\ \frac{d^2u_3}{d\eta^2} \end{bmatrix}, \qquad (28)$$

where $\mathbf{u} = [u_1, u_2, u_3]^T$ and

$$\mathbf{I}_{2m} = \begin{bmatrix} I_{21}(\eta_2) & I_{22}(\eta_2) & I_{23}(\eta_2) & \eta_2 & 1 & 0 & 0 \end{bmatrix}. \qquad (29)$$

In a similar manner to the first-order derivative approximation, one can derive the second-order derivative approximation at the interior node

$$\begin{bmatrix} -\mathbf{D}_2(4) & 0 & -\mathbf{D}_2(5) \end{bmatrix}\mathbf{u}' + \begin{bmatrix} -\mathbf{D}_2(6) & 1 & -\mathbf{D}_2(7) \end{bmatrix}\mathbf{u}'' = \mathbf{D}_2(1:3)\mathbf{u}, \quad (30)$$

where $\mathbf{u}' = \left[\frac{du_1}{d\eta}, \frac{du_2}{d\eta}, \frac{du_3}{d\eta}\right]^T$ and $\mathbf{u}'' = \left[\frac{d^2u_1}{d\eta^2}, \frac{d^2u_2}{d\eta^2}, \frac{d^2u_3}{d\eta^2}\right]^T$.

At the boundary nodes, e.g. $\eta = \eta_1$, we employ the same special stencil, e.g. $\{\eta_1, \eta_2, \eta_3, \eta_4\}$, and extra information, e.g. $\frac{du_2}{d\eta}$ and $\frac{d^2u_2}{d\eta^2}$, used in the approximation of the first-order derivatives. Therefore, approximate expression for the second-order derivative at the boundary point in the physical space is obtained by simply substituting (23) into (7) and taking $\eta = \eta_1$

$$\frac{d^2u_1}{d\eta^2} = \underbrace{\mathbf{I}_{2b}\mathbf{C}_{sp}^{-1}}_{\mathbf{D}_{2sp}}\begin{bmatrix} \mathbf{u} \\ \frac{du_2}{d\eta} \\ \frac{d^2u_2}{d\eta^2} \end{bmatrix}, \qquad (31)$$

9

where $\mathbf{u} = [u_1, u_2, u_3, u_4]^T$ and

$$\mathbf{I}_{2b} = \begin{bmatrix} I_{21}(\eta_1) & I_{22}(\eta_1) & I_{23}(\eta_1) & I_{24}(\eta_1) & \eta_1 & 1 & 0 & 0 \end{bmatrix}. \quad (32)$$

In a similar manner, one can derive the second-order derivative approximation at the boundary node

$$\begin{bmatrix} 0 & -\mathbf{D}_{2sp}(5) & 0 & 0 \end{bmatrix} \mathbf{u}' + \begin{bmatrix} 1 & -\mathbf{D}_{2sp}(6) & 0 & 0 \end{bmatrix} \mathbf{u}'' = \mathbf{D}_{2sp}(1:4)\mathbf{u}, \quad (33)$$

where $\mathbf{u}' = \left[\frac{du_1}{d\eta}, \frac{du_2}{d\eta}, \frac{du_3}{d\eta}, \frac{du_4}{d\eta} \right]^T$ and $\mathbf{u}'' = \left[\frac{d^2 u_1}{d\eta^2}, \frac{d^2 u_2}{d\eta^2}, \frac{d^2 u_3}{d\eta^2}, \frac{d^2 u_4}{d\eta^2} \right]^T$.

3.3. Matrix assembly for first- and second-order derivative approximations

The IRBF system on a grid line for the first-order derivative is obtained by letting the interior node take values from 2 to $(n_\eta - 1)$ in (18) and making use of (27) for the boundary nodes 1 and n_η. In a similar manner, the IRBF system on a grid line for the second-order derivative is obtained by letting the interior node take values from 2 to $(n_\eta - 1)$ in (30) and making use of (33) for the boundary nodes 1 and n_η. The resultant matrix assembly is expressed as

$$\underbrace{\begin{bmatrix} \mathbf{A}_1 & \mathbf{B}_1 \\ \mathbf{A}_2 & \mathbf{B}_2 \end{bmatrix}}_{\text{Coefficient matrix}} \begin{bmatrix} \mathbf{u}'^n \\ \mathbf{u}''^n \end{bmatrix} = \begin{bmatrix} \mathbf{R}_1 \\ \mathbf{R}_2 \end{bmatrix} \mathbf{u}^n, \quad (34)$$

where $\mathbf{A}_1, \mathbf{A}_2, \mathbf{B}_1, \mathbf{B}_2, \mathbf{R}_1$, and $\mathbf{R}_2$ are $n_\eta \times n_\eta$ matrices; $\mathbf{u}'^n = \left[u_1'^n, u_2'^n, ..., u_{n_\eta}'^n \right]^T$; $\mathbf{u}''^n = \left[u_1''^n, u_2''^n, ..., u_{n_\eta}''^n \right]^T$; and $\mathbf{u}^n = \left[u_1^n, u_2^n, ..., u_{n_\eta}^n \right]^T$. The coefficient matrix is sparse with diagonal sub-matrices. Solving (34) yields

$$\mathbf{u}'^n = \mathbf{D}_\eta \mathbf{u}^n, \quad (35)$$

$$\mathbf{u}''^n = \mathbf{D}_{\eta\eta} \mathbf{u}^n, \quad (36)$$

where $\mathbf{D}_\eta$ and $\mathbf{D}_{\eta\eta}$ are first- and second-order differential matrices, respectively.

It can be seen that the derivative at a grid point is computed using all nodal variable values on the two grid lines intersecting at that point. Unlike the spectral method, the present scheme can be directly applied to problems of irregular shapes, where the Cartesian grid used can be uniform or non-uniform. In the case of the Dirichlet boundary conditions, by collocating the PDE at the interior grid nodes and making use of (35) and (36), a determined system of algebraic equations is obtained, which can be solved for the field variable at the interior grid nodes. It is noted that with derivatives depending on nodal variable values on a grid line, the sparseness level of the global system matrix is reduced in comparison with that of the coefficient matrix in equation (34).

We note that the use of fourth-order IRBFs here (i.e. CCIRBF) is more straightforward to include first- and second-order derivative values than the use of second-order IRBFs [19, 37]. The former involves only one conversion matrix while there are two conversion matrices required for the latter: one taking extra first-order derivative values and the other taking second-order derivative values.

10

4. Preconditioning technique for the CCIRBF

To improve the stability of the CCIRBF in the large value range of β, we construct a new equivalent conversion system by multiplying a preconditioning matrix $\mathbf{C}^{*-1}$ to both sides of the original conversion system (10) as follows.

$$\mathbf{C}^{*-1} \begin{bmatrix} u_1 \\ u_2 \\ u_3 \\ \frac{du_1}{d\eta} \\ \frac{du_3}{d\eta} \\ \frac{d^2 u_1}{d\eta^2} \\ \frac{d^2 u_3}{d\eta^2} \end{bmatrix} = \underbrace{\mathbf{C}^{*-1}\mathbf{C}}_{\mathbf{C}_p} \begin{bmatrix} w_1 \\ w_2 \\ w_3 \\ c_1 \\ c_2 \\ c_3 \\ c_4 \end{bmatrix}, \tag{37}$$

where $\mathbf{C}$ is the original conversion matrix in (10); $\mathbf{C}^{*-1}$ is the preconditioning matrix which has exactly the same form as the original conversion matrix $\mathbf{C}$ but uses a different value of β. Usually, β used in $\mathbf{C}^{*-1}$ is taken to be small, for example $\beta = 10$, so that its corresponding condition number is in a well-behaved range; and $\mathbf{C}_p$ is a new conversion matrix. This numerical treatment is expected to bypass the ill-condition problems when β in the original conversion matrix $\mathbf{C}$ becomes large (but not go to infinity as the information in $\mathbf{C}$ is lost in this limit due to the current use of finite (double) precision).

Solving (37) yields

$$\begin{bmatrix} w_1 \\ w_2 \\ w_3 \\ c_1 \\ c_2 \\ c_3 \\ c_4 \end{bmatrix} = \mathbf{C}_p^{-1}\mathbf{C}^{*-1} \begin{bmatrix} u_1 \\ u_2 \\ u_3 \\ \frac{du_1}{d\eta} \\ \frac{du_3}{d\eta} \\ \frac{d^2 u_1}{d\eta^2} \\ \frac{d^2 u_3}{d\eta^2} \end{bmatrix}. \tag{38}$$

In a similar manner detailed in Section 3, one is able to derive the first- and second-order derivative approximations with the new conversion system. It is noted that the proposed preconditioning technique is only needed when one implements the CCIRBF in the large range of β where the ill-condition problems occur. In the small range of β, for example $\beta = \{1, 2, ..., 100\}$, the "pure" CCIRBF normally works fine.

5. Numerical examples

Various kinds of differential problems, including ODEs, Poisson, Burgers, convection-diffusion and Navier-Stokes equations, are employed to verify the proposed preconditioning technique which is developed to enhance the working

11

We evaluate the performance of the present schemes through the following measures

i. The root mean square error (RMS) is defined as

$$RMS = \sqrt{\frac{\sum_{i=1}^{N} \left(u_i - \overline{u}_i\right)^2}{N}}, \qquad (39)$$

where u_i and $\overline{u}_i$ are the computed and exact values of the solution u at the i-th node, respectively; and N is the number of nodes over the whole domain.

ii. The global convergence rate, α, with respect to the grid refinement is defined through

$$Error(h) \approx \gamma h^\alpha = O(h^\alpha). \qquad (40)$$

where h is the grid size; and γ and α are exponential model's parameters.

For comparison purposes, in Sections 5.1 and 5.2, we also implement the global DRBF scheme of [5, 6], the CIRBF scheme of [37], and the standard central Finite Difference Method (FDM) for numerical solutions. It is noted that the proposed preconditioning technique described in Section 4 is also applied for the CIRBF-Precond version.

For fluid flow examples in Sections 5.1 to 5.5 and 5.8, we choose a large shape parameter, $\beta = 1000$, for the original conversion matrix $\mathbf{C}$ and a small shape parameter, $\beta = 10$, for the preconditioning matrix $\mathbf{C*}^{-1}$; and in the examples of Taylor-Green vortex flows, i.e. Sections 5.6 and 5.7, we choose a large shape parameter, $\beta = 500$, for the original conversion matrix $\mathbf{C}$ and a small shape parameter, $\beta = 10$, for the preconditioning matrix $\mathbf{C*}^{-1}$. We employ the fully coupled procedure which was detailed in [18] to calculate Navier-Stokes equations in Sections 5.6 to 5.8.

In this work, calculations are done with a Dell computer Optiplex 9010 version 2013. Its specifications are intel(R) core(TM) i7-3770 CPU 3.40 GHz 3.40 GHz, memory(RAM) of 8GB(7.89 usable) and 64-bit operating system. The Matlab(R) version 2014 is utilised.

5.1. Second-order ODE

In order to study the 1D spatial accuracy of the present CCIRBF approximation schemes, we consider the following equations

$$\frac{d^2 u}{dx^2} = -\pi^2 sin(\pi x), \qquad (41)$$

$$\frac{du}{dx} = \pi cos(\pi x), \qquad (42)$$

on a domain $[0, 1]$, subjected to the Dirichlet boundary condition derived from the following exact solution

$$\overline{u} = sin(\pi x). \qquad (43)$$

12

Nodal values of both first- and second-order derivatives of u are computed. The calculations are carried out on uniform grids of $\{11, 51, 101\}$. We employ a wide range of β, $\{1, 101, 201, ..., 2001\}$. Figures 5, 8, and 11 illustrate the effect of β on the condition number of the conversion matrix, where we can see that the present CCIRBF-Precond has much lower condition numbers than the "pure" CCIRBF. Figures 6, 7, 9, 10, 12, and 13 show that the present CCIRBF-Precond scheme is more accurate than the DRBF, CIRBF and CIRBF-Precond schemes for computing $\frac{du}{dx}$ and $\frac{d^2u}{dx^2}$ in the large value range of β. The improvement of several orders of magnitude can be observed, e.g. Figure 13. These Figures also show that the present preconditioning technique leads to a significant improvement in the matrix condition number of the CCIRBF and the CIRBF over the large value range of β.

To study the computational efficiency of the CCIRBF and the CIRBF, we employ different sets of grid points with an increment of 10 (i.e. $\{11, 21, ...\}$) and carry out the simulation until the solution accuracy achieves a target RMS level of 5×10^{-6}. Results obtained are shown in Figure 14, indicating that the present scheme CCIRBF uses smaller numbers of grids and takes much less time to reach the target accuracy than the CIRBF. The ratio of the elapsed time of the CCIRBF to that of the CIRBF is about 1/20 as the grid required is 41 for the former and 661 for the latter.
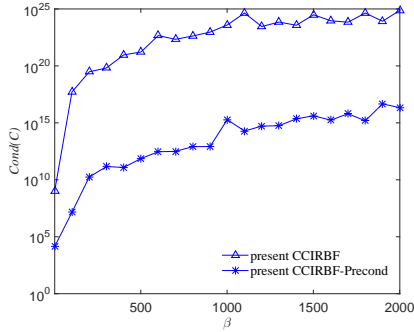
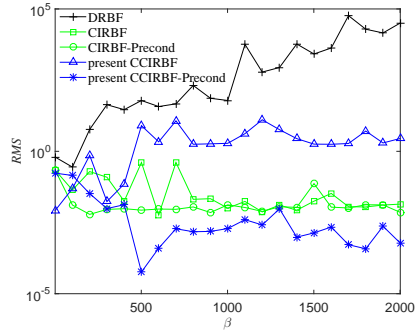Figure 5: Second-order ODE, $nx = 11$: The effect of β on the condition number of the conversion matrix.

Figure 6: Second-order ODE, $nx = 11$: The effect of β on the solution accuracy RMS of first-order derivative approximations.
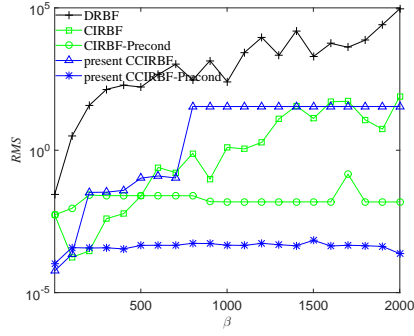
Figure 7: Second-order ODE, $nx = 11$: The effect of β on the solution accuracy RMS of second-order derivative approximations.
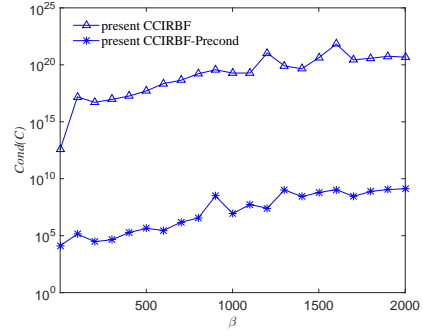

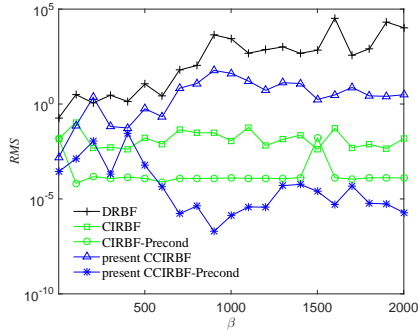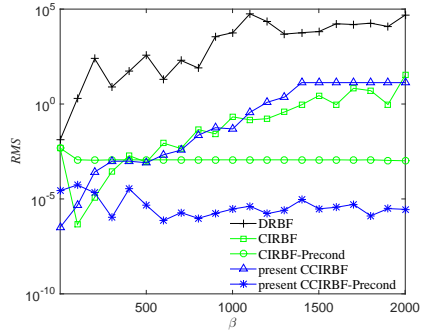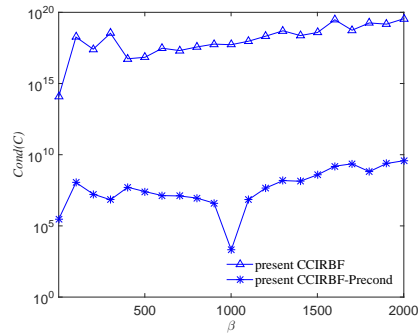Figure 8: Second-order ODE, $nx = 51$: The effect of β on the condition number of the conversion matrix.
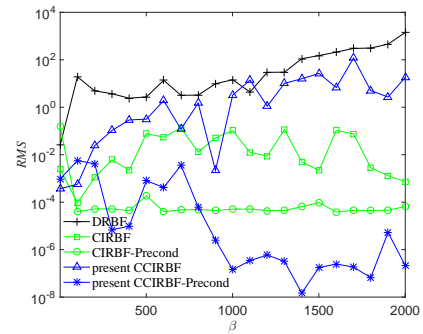

Figure 9: Second-order ODE, $nx = 51$: The effect of β on the solution accuracy RMS of first-order derivative approximations.

Figure 10: Second-order ODE, $nx = 51$: The effect of β on the solution accuracy RMS of second-order derivative approximations.

Figure 11: Second-order ODE, $nx = 101$: The effect of β on the condition number of the conversion matrix.

Figure 12: Second-order ODE, $nx = 101$: The effect of β on the solution accuracy RMS of first-order derivative approximations.
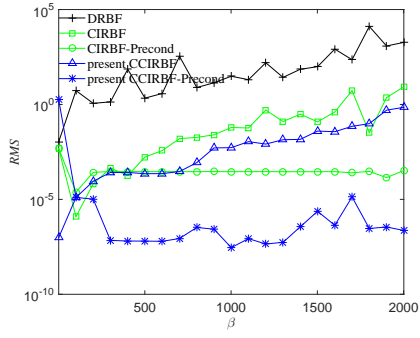
14

Figure 13: Second-order ODE, $nx = 101$: The effect of β on the solution accuracy RMS of second-order derivative approximations.
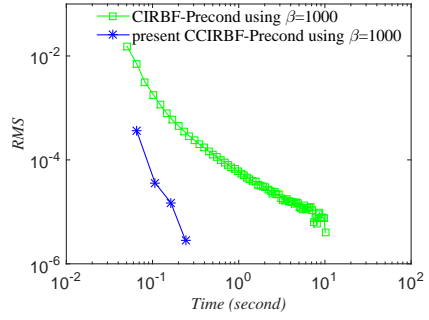
Figure 14: Second-order ODE, $\{11, 21, ...\}$: The computational cost to achieve the target accuracy of 5×10^{-6}. The final grid is 661 for the CIRBF and 41 for the CCIRBF.

15

5.2. Poisson equation

In order to study the 2D spatial accuracy of the present CCIRBF approximation schemes, we consider the following Poisson equation

$$\frac{d^2u}{dx_1^2} + \frac{d^2u}{dx_2^2} = -2\pi^2 \cos(\pi x_1)\cos(\pi x_2), \tag{44}$$

on a square domain $[0, 1]^2$, subjected to the Dirichlet boundary condition derived from the following exact solution

$$\overline{u} = \cos(\pi x_1)\cos(\pi x_2). \tag{45}$$

The calculations are carried out on uniform grids of $\{11 \times 11, 51 \times 51, 101 \times 101\}$. A set of β of $\{1, 101, 201, ..., 2001\}$ is chosen. As in the case of the second-order ODE (i.e. Section 5.1), the present CCIRBF-Precond scheme outperforms the DRBF, CIRBF and CIRBF-Precond schemes in terms of the solution accuracy and stability (Figures 15 to 17). These Figures also indicate that the stability of the CCIRBF and the CIRBF is much improved with the present preconditioning technique.
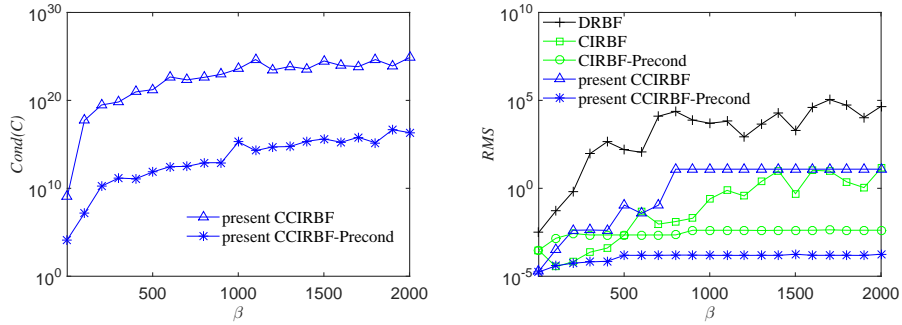

Figure 15: Poisson equation, 11×11: The effect of β on the condition number of the conversion matrix (left) and on the solution accuracy RMS (right).

To study the computational efficiency of the CCIRBF and the CIRBF, we increase the density of grids as $\{11 \times 11, 21 \times 21, ...\}$ until the solution accuracy achieves a target RMS level of 5×10^{-5}. Figure 18 shows that the present scheme CCIRBF uses much smaller numbers of grids and takes much less time to reach the target accuracy than the CIRBF. Finally, Figure 19 shows the spy-plot of a typical coefficient matrix.
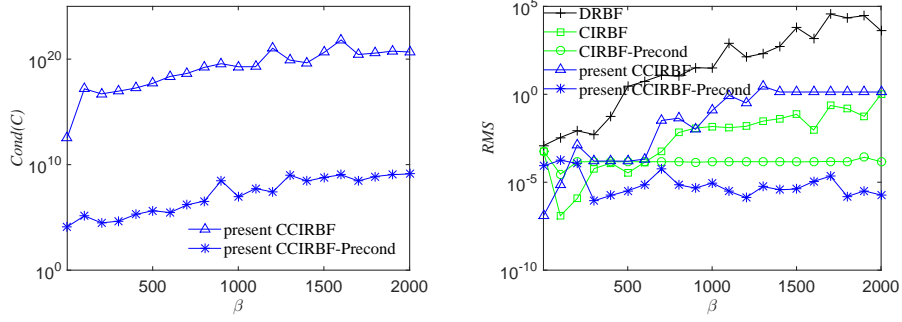
Figure 16: Poisson equation, 51×51: The effect of β on the condition number of the conversion matrix (left) and on the solution accuracy RMS (right).
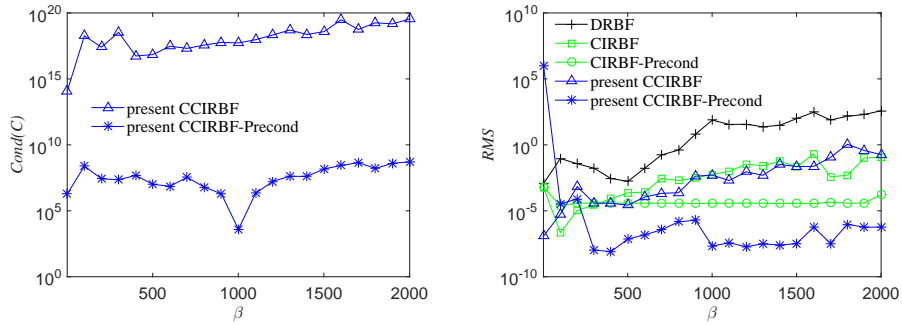

Figure 17: Poisson equation, 101×101: The effect of β on the condition number of the conversion matrix (left) and on the solution accuracy RMS (right).
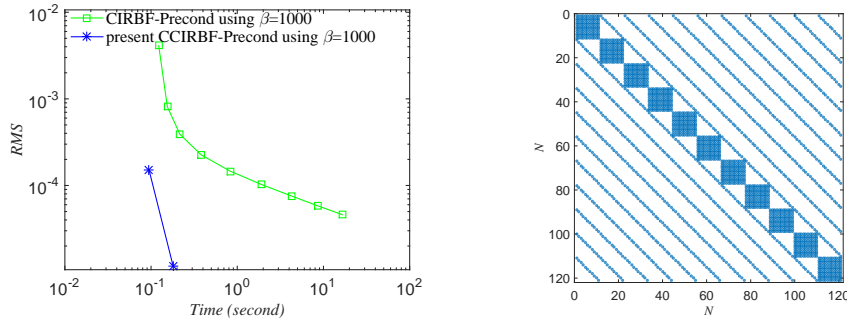

Figure 18: Poisson equation, $\{11 \times 11, 21 \times 21, ...\}$: The computational cost to achieve the target accuracy of 5×10^{-5}. The final grid is 91×91 for the CIRBF and 21×21 for the CCIRBF.

Figure 19: Poisson equation, 11×11, $\beta = 1000$ ($11 \times 11 = 121$ unknowns): The spy-plot of the 121×121 coefficient matrix with 2541 non-zero entries (approximately 17.4% of $121 \times 121 = 14641$ entries).

5.3. Heat equation

By selecting the following heat equation, the performance of the present CCIRBF scheme can be studied for the diffusive term only

$$\frac{\partial u}{\partial t} = \frac{\partial^2 u}{\partial x^2}, \quad a \leq x \leq b, \quad t \geq 0, \tag{46}$$

$$u(x, 0) = u_0(x), \quad a \leq x \leq b, \tag{47}$$

$$u(a, t) = u_{\Gamma_1}(t) \quad \text{and} \quad u(b, t) = u_{\Gamma_2}(t), \quad t \geq 0, \tag{48}$$

where u and t are the temperature and time, respectively; and $u_0(x)$, $u_{\Gamma_1}(t)$, and $u_{\Gamma_2}(t)$ are prescribed functions. The temporal discretisation of (46) with the Crank-Nicolson scheme gives

$$\frac{u^n - u^{n-1}}{\Delta t} = \frac{1}{2} \left\{ \frac{\partial^2 u^n}{\partial x^2} + \frac{\partial^2 u^{n-1}}{\partial x^2} \right\}, \tag{49}$$

where the superscript n denotes the current time level. (49) can be rewritten as

$$\left\{ 1 - \frac{\Delta t}{2} \frac{\partial^2}{\partial x^2} \right\} u^n = \left\{ 1 + \frac{\Delta t}{2} \frac{\partial^2}{\partial x^2} \right\} u^{n-1}. \tag{50}$$

Consider (46) on a segment $[0, \pi]$ with the initial and boundary conditions

$$u(x, 0) = \sin(2x), \quad 0 < x < \pi. \tag{51}$$

$$u(0, t) = u(\pi, t) = 0, \quad t \geq 0. \tag{52}$$

The exact solution of this problem is

$$\overline{u}(x, t) = \sin(2x)e^{-4t}. \tag{53}$$

The spatial accuracy of the proposed scheme is tested on various uniform grids $\{11, 21, ..., 101\}$. We employ here a small time step, $\Delta t = 10^{-6}$, to minimise the effect of the approximation error in time. The solution is computed at $t = 0.0125$. Figure 20 shows that the CCIRBF-Precond using $\beta = 1000$ outperforms the FDM in terms of both the solution accuracy and the convergence rate.
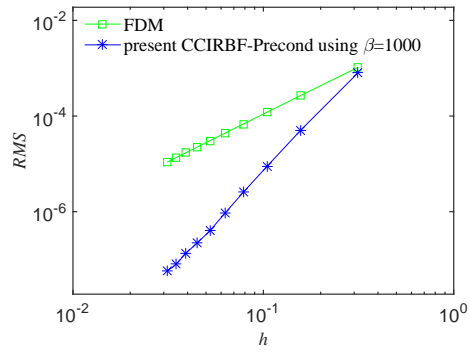
18

Figure 20: Heat equation, $\{11, 21, ..., 101\}$, $Re = 100$, $\Delta t = 10^{-6}$, $t = 0.0125$: The effect of the grid size h on the solution accuracy RMS. The solution converges as $O(h^{1.98})$ for the FDM and $O(h^{4.21})$ for the CCIRBF-Precond scheme.

5.4. Burgers equation

With Burgers equation, the performance of the present CCIRBF scheme can be investigated for both the convective and diffusive terms

$$\frac{\partial u}{\partial t} + u \frac{\partial u}{\partial x} = \frac{1}{Re} \frac{\partial^2 u}{\partial x^2}, \quad a \leq x \leq b, \quad t \geq 0, \tag{54}$$

$$u(x,0) = u_0(x), \quad a \leq x \leq b, \tag{55}$$

$$u(a,t) = u_{\Gamma_1}(t) \quad \text{and} \quad u(b,t) = u_{\Gamma_2}(t), \quad t \geq 0, \tag{56}$$

where $Re > 0$ is the Reynolds number; and $u_0(x)$, $u_{\Gamma_1}(t)$, and $u_{\Gamma_2}(t)$ are prescribed functions.

The temporal discretisations of (54) using the Adams-Bashforth scheme for the convective term and Crank-Nicolson scheme for the diffusive term, result in

$$\frac{u^n - u^{n-1}}{\Delta t} + \left\{ \frac{3}{2} \left(u \frac{\partial u}{\partial x} \right)^{n-1} - \frac{1}{2} \left(u \frac{\partial u}{\partial x} \right)^{n-2} \right\} = \frac{1}{2Re} \left\{ \frac{\partial^2 u^n}{\partial x^2} + \frac{\partial^2 u^{n-1}}{\partial x^2} \right\}, \tag{57}$$

or

$$\left\{ 1 - \frac{\Delta t}{2Re} \frac{\partial^2}{\partial x^2} \right\} u^n = \left\{ 1 + \frac{\Delta t}{2Re} \frac{\partial^2}{\partial x^2} \right\} u^{n-1} - \Delta t \left\{ \frac{3}{2} \left(u \frac{\partial u}{\partial x} \right)^{n-1} - \frac{1}{2} \left(u \frac{\partial u}{\partial x} \right)^{n-2} \right\}. \tag{58}$$

The problem is considered on a segment $0 \leq x \leq 1$, $t \geq 0$ in the form [40]

$$\overline{u}(x,t) = \frac{\alpha_0 + \mu_0 + (\mu_0 - \alpha_0) \exp(\lambda)}{1 + \exp(\lambda)}, \tag{59}$$

where $\lambda = \alpha_0 Re(x - \mu_0 t - \beta_0)$, $\alpha_0 = 0.4$, $\beta_0 = 0.125$, $\mu_0 = 0.6$, and $Re = 100$.

The initial and boundary conditions can be derived from the analytic solution (59). The calculations are carried out on a set of uniform grids $\{11, 21, ..., 101\}$. The time step $\Delta t = 10^{-6}$ is chosen. The errors of the solution are calculated at the time $t = 0.0125$. Figure 21 displays that the present CCIRBF-Precond using $\beta = 1000$ has much lower errors than the FDM. Also, its convergence rate is much better than that of the FDM.
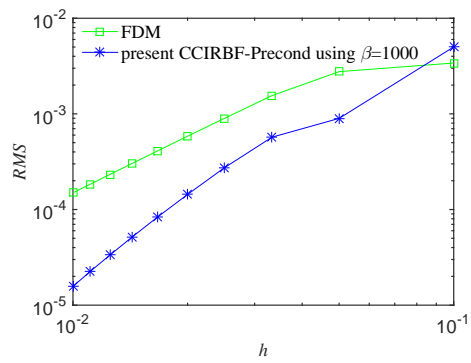
20

Figure 21: Burgers equation, $\{11, 21, ..., 101\}$, $Re = 100$, $\Delta t = 10^{-6}$, $t = 0.0125$: The effect of the grid size h on the solution accuracy RMS. The solution converges as $O(h^{1.48})$ for the FDM and $O(h^{2.47})$ for the CCIRBF-Precond scheme.

21

5.5. Convection-diffusion equations

To study the performance of the present CCIRBF approximation in simulating convection diffusion problems, we employ the Alternating Direction Implicit (ADI) procedure which was detailed in [19]. A two-dimensional unsteady convection-diffusion equation for a variable u is expressed as follows.

$$\frac{\partial u}{\partial t} + c_x \frac{\partial u}{\partial x} + c_y \frac{\partial u}{\partial y} = d_x \frac{\partial^2 u}{\partial x^2} + d_y \frac{\partial^2 u}{\partial y^2} + f_b, \quad (x,y,t) \in \Omega \times [0,T], \quad (60)$$

subject to the initial condition

$$u(x,y,0) = u_0(x,y), \quad (x,y) \in \Omega, \quad (61)$$

and the Dirichlet boundary condition

$$u(x,y,t) = u_\Gamma(x,y,t), \quad (x,y) \in \Gamma, \quad (62)$$

where Ω is a two-dimensional rectangular domain; Γ is the boundary of Ω; $[0,T]$ is the time interval; f_b is the driving function; u_0 and u_Γ are some given functions; c_x and c_y are the convective velocities; and d_x and d_y are the diffusive coefficients.

In this work, we consider $f_b = 0$, in a square $\Omega = [0,2]^2$ with the following analytic solution [41]

$$\overline{u}(x,y,t) = \frac{1}{4t+1} exp\left[-\frac{(x-c_x t-0.5)^2}{d_x(4t+1)} - \frac{(y-c_y t-0.5)^2}{d_y(4t+1)}\right]. \quad (63)$$

From (63), one can derive the initial and boundary conditions. We consider two sets of parameters [42]

Case I: $c_x = c_y = 0.8$, $d_x = d_y = 0.01$, $t = 1.25$, $\Delta t = 2.5E-4$.

Case II: $c_x = c_y = 80$, $d_x = d_y = 0.01$, $t = 0.0125$, $\Delta t = 2.5E-6$.

The corresponding Peclet number is thus $Pe = 2$ for case I and $Pe = 200$ for case II. To study the accuracy of the solution with the grid refinement, we employ sets of uniform grids as shown in Figures 22 and 23. The results in these Figures show that the accuracy and the convergence rate of the proposed CCIRBF-Precond using $\beta = 1000$ are much better than those of the FDM. For case I, the convergence rates are $O(h^{3.38})$ and $O(h^{1.55})$ for the CCIRBF and the FDM, respectively. For case II, the convergence rates are $O(h^{2.71})$ and $O(h^{0.85})$ for the CCIRBF and the FDM, respectively.
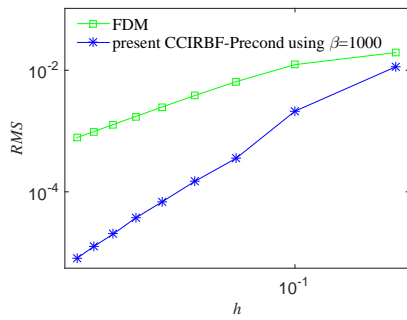
Figure 22: Convection-diffusion equation, $\{11 \times 11, 21 \times 21, ..., 91 \times 91\}$, case I: The effect of the grid size h on the solution accuracy RMS. The solution converges as $O(h^{1.55})$ for the FDM and $O(h^{3.38})$ for the CCIRBF-Precond scheme.
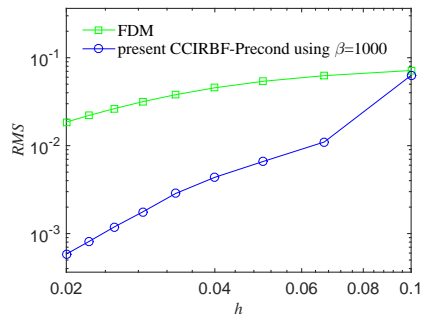
Figure 23: Convection-diffusion equation, $\{21 \times 21, 31 \times 31, ..., 101 \times 101\}$, case II: The effect of the grid size h on the solution accuracy RMS. The solution converges as $O(h^{0.85})$ for the FDM and $O(h^{2.71})$ for the CCIRBF-Precond scheme.

To study the performance of the present CCIRBF approximation in simulating viscous flows in a rectangular domain, we consider a transient viscous flow problem, namely Taylor-Green vortex which is governed by Navier-Stokes equations. The problem has the analytical solutions as follows [43].

$$\overline{u}(x_1, x_2, t) = -\cos(kx_1)\sin(kx_2)\exp(-2k^2t/Re), \tag{64}$$

$$\overline{v}(x_1, x_2, t) = \sin(kx_1)\cos(kx_2)\exp(-2k^2t/Re), \tag{65}$$

$$\overline{p}(x_1, x_2, t) = -1/4\left\{\cos(2kx_1) + \cos(2kx_2)\right\}\exp(-4k^2t/Re), \tag{66}$$

where $0 \le x_1, x_2 \le 2\pi$. Calculations are carried out for $k = 2$ on a set of uniform grid, $\{11 \times 11, 21 \times 21, ..., 51 \times 51\}$. A fixed time step $\Delta t = 0.002$ and $Re = 100$ are employed. Numerical solutions are computed at $t = 2$. The exact solution, i.e. equations (64)-(66), provides the initial field at $t = 0$ and the time-dependent boundary conditions. Table 1 shows the accuracy comparison between the present scheme and the High-Order Compact (HOC) finite difference scheme of [43] (fourth-order). It is seen that the present scheme is superior to the HOC in terms of both the level of accuracy and the convergence rate. The solutions for the u- and v-velocities and for pressure converge, respectively, as $O(h^{3.91})$ and $O(h^{3.81})$ for the present method, and only $O(h^{2.92})$ and $O(h^{3.28})$ for the HOC.

Table 1: Taylor-Green vortex, rectangular domain: RMS errors and convergence rates.

Grid	present CCIRBF using $\beta = 500$		
	u-error	v-error	p-error
11×11	9.0757315E-02	9.0757322E-02	2.3542625E-01
21×21	3.8338024E-03	3.8338114E-03	1.3288235E-02
31×31	1.0201809E-03	1.0201870E-03	3.3851835E-03
41×41	3.6194151E-04	3.6194102E-04	1.4603595E-03
51×51	1.5492043E-04	1.5482812E-04	4.1378984E-04
Rate	$O(h^{3.91})$	$O(h^{3.91})$	$O(h^{3.81})$
	HOC [43]		
Grid	u-error	v-error	p-error
11×11	7.0070489E-02	7.0070489E-02	1.0764149E-01
21×21	9.0692193E-03	9.0692193E-03	1.0567607E-02
31×31	2.8851487E-03	2.8851487E-03	2.9103288E-03
41×41	1.2238736E-03	1.2238736E-03	1.1356134E-03
51×51	6.3063026E-04	6.3063026E-04	5.3933641E-04
Rate	$O(h^{2.92})$	$O(h^{2.92})$	$O(h^{3.28})$

5.7. Taylor-Green vortex in non-rectangular domain

In order to analyse the performance of the present CCIRBF approximation scheme in solving the transient viscous flow in a non-rectangular domain, we consider the case of an array of decaying vortices with the analytical solutions [18] described by

$$\overline{u}(x_1, x_2, t) = \sin(\pi x_1)\cos(\pi x_2)\exp(-2\pi^2 t/Re), \tag{67}$$

$$\overline{v}(x_1, x_2, t) = -\sin(\pi x_2)\cos(\pi x_1)\exp(-2\pi^2 t/Re), \tag{68}$$

$$\overline{p}(x_1, x_2, t) = 1/2\left\{\cos^2(\pi x_2) - \sin^2(\pi x_1)\right\}\exp(-4\pi^2 t/Re). \tag{69}$$

The flow is computed in a circular domain with radius of unity and centred at the origin of the coordinate system. The problem domain is embedded in a uniform Cartesian grid on $\Omega = [-1.5, 1.5]^2$ and the grid nodes exterior to the domain are removed. The interior nodes falling within a small distance $\delta = h/8$, where h is the grid size, to the boundary will also be discarded [44]. The boundary nodes are generated through the intersection of the grid lines and the boundary as demonstrated in Figure 24.
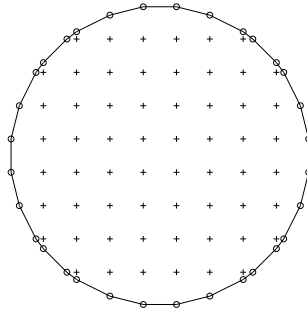

Figure 24: Taylor-Green vortex, non-rectangular domain, spatial discretisation: + represents interior nodes; and ∘ represents boundary nodes.

The calculations are carried out using several uniform grids, $\{10 \times 10, 20 \times 20, ..., 50 \times 50\}$. The Reynolds number is set to be $Re = 5$ and numerical solutions are computed at $t = 0.3$ using a fixed time step $\Delta t = 0.001$. The initial field at $t = 0$ and time-dependent boundary conditions are given by (67)-(69). Table 2 illustrates the accuracy comparison between the present scheme and the CIRBF approach of [18]. It is observed that errors produced by the present scheme are much lower than those generated by the CIRBF.

25

Table 2: Taylor Green vortex, non-rectangular domain: RMS errors and convergence rates.

Grid	present CCIRBF using $\beta = 500$		
	u-error	v-error	p-error
10×10	6.7854399E-03	7.3789723E-03	1.5666056E-02
20×20	7.3935223E-04	5.3269646E-04	7.4691913E-03
30×30	1.3671917E-04	1.1479088E-04	2.5417428E-04
40×40	4.5332629E-05	3.4903187E-05	3.1245155E-04
50×50	1.7119756E-05	1.6100433E-05	8.5671434E-05
Rate	$O(h^{3.53})$	$O(h^{3.63})$	$O(h^{3.20})$
Grid	CIRBF using $\beta = 40$ [18]		
	u-error	v-error	p-error
10×10	5.0940713E-02	3.9890094E-02	9.5986185E-02
20×20	1.1003665E-03	7.9266552E-04	2.2013746E-03
30×30	9.7670238E-05	8.1362620E-05	5.1711179E-04
40×40	5.8426984E-05	2.8665169E-05	2.1616129E-04
50×50	3.3759336E-05	2.3569385E-05	1.4680716E-04
Rate	$O(h^{4.44})$	$O(h^{4.59})$	$O(h^{3.88})$

5.8. Irregular bottom lid driven cavity

The lid driven cavity with a deformed base presented in [18, 45, 46, 47]
is chosen to validate the performance of the present approximation scheme in
simulating fluid flow problems in an irregular domain. The base is deformed
sinusoidally with an amplitude of 10 percent of the base. The computational
domain and boundary conditions are illustrated in Figure 25.
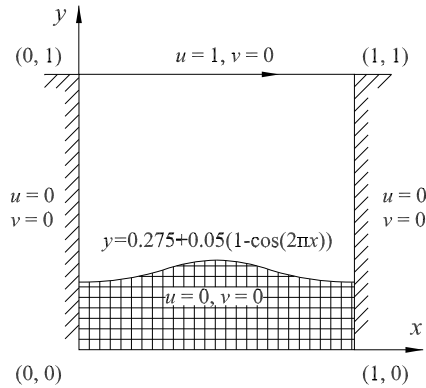

Figure 25: Irregular bottom lid driven cavity: problem configuration and boundary conditions.

The interior and boundary nodes are generated in a similar manner described
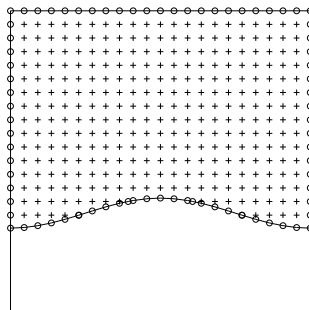in Section 5.7. The spatial discretisation is shown in Figure 26.

Figure 26: Irregular bottom lid driven cavity, spatial discretisation: + represents interior
nodes; ○ represents boundary nodes.

A range of uniform grids, $\{53 \times 53, 63 \times 63, 83 \times 83, 93 \times 93\}$ is employed in
the simulation. A fixed time step and Reynolds number are chosen to be $\Delta t =$
0.001 and $Re = 1000$, respectively. The results obtained by the present method
are compared with those reported in [18, 46, 47], where appropriate. From the

27

literature, the Finite Volume Method (FVM) results using the well-tested body-fitted coordinate formulation and the dense grid of 121×121 presented in [46] have been considered as "Benchmark" results for comparison purposes.

Table 3 shows the present results for the extrema of the vertical and horizontal velocity profiles along the vertical centreline of the cavity. With relatively coarse grids, the results obtained by the present scheme are very comparable with other schemes using much denser grids. Although good numerical results are acquired, the effects of irregular boundaries on the solution accuracy and stability are still not theoretically explained, and further studies are needed.

Figure 27 displays horizontal and vertical velocity profiles along the vertical centreline for different grid sizes, where a grid convergence of the present scheme is obviously observed (i.e. the present solution approaches the benchmark solution with a fast rate as the grid density is increased). The present scheme effectively achieves the benchmark results with a grid of only 83×83 in comparison with the grid of 121×121 used to obtain the benchmark results in [46]. In addition, the present results with a grid of only 53×53 outperform those of [47] using the grid of 100×100.
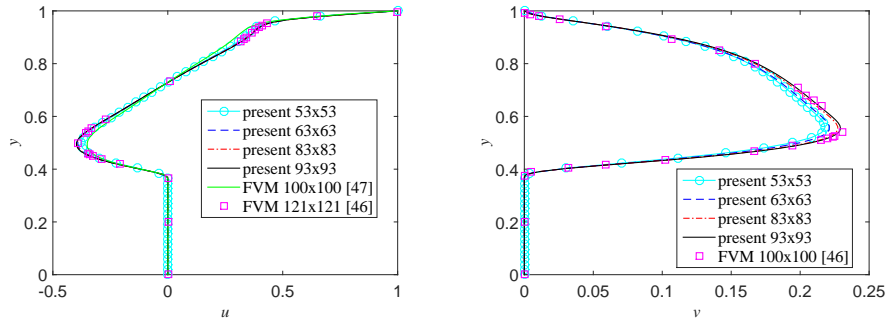

Figure 27: Irregular bottom lid driven cavity, $\beta = 1000$, $Re = 1000$: Profiles of the u-velocity (left) and v-velocity (right) along the vertical centreline as the grid density increases. It is noted that the curves for the last two grids are indistinguishable and in good agreement with the benchmark results of [46].

To exhibit contour plots of the flow, we employ the grid of 83×83. Figures 28 and 29 show streamlines (which are derived from the velocity) and pressure deviation contours, respectively. These plots are in close agreement with those reported in the literature. Additionally, Figure 30 shows the iso-vorticity lines of the present simulation.

Table 3: Irregular bottom lid driven cavity, $\beta = 1000$, $Re = 1000$: Extrema of the vertical and horizontal velocity profiles along the vertical centreline of the cavity.

| Method	Grid	u_{min}	y_{min}	v_{max}	y_{max}
Present CCIRBF	53×53	-0.3781442	0.4975	0.2180640	0.5601
Present CCIRBF	63×63	-0.3924106	0.4959	0.2214069	0.5563
Present CCIRBF	83×83	-0.3958749	0.4951	0.2274348	0.5547
Present CCIRBF	93×93	-0.3979039	0.4949	0.2292693	0.5549
CIRBF (u, v, p) [18]	53×53	-0.3695975	0.4989	0.2165344	0.5638
CIRBF (u, v, p) [18]	63×63	-0.3847773	0.4967	0.2239138	0.5589
CIRBF (u, v, p) [18]	83×83	-0.3950552	0.4953	0.2282167	0.5555
CIRBF (u, v, p) [18]	93×93	-0.3972010	0.4950	0.2286893	0.5548
FVM[a] (u, v, p) [47]	100×100	$\approx$ -0.3524	$\approx$ 0.4929	—	—
Benchmark FVM[a] (u, v, p) [46]	121×121	$\approx$ -0.3808	$\approx$ 0.5017	$\approx$ 0.2362	$\approx$ 0.5610

[a] FVM results extracted from Figures in [46, 47]
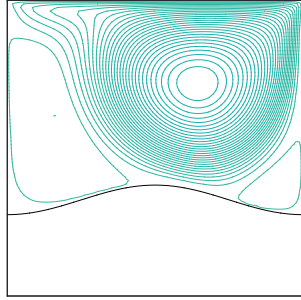
Figure 28: Irregular bottom lid driven cavity, $\beta = 1000$, $Re = 1000$: Streamlines of the flow with the grid of 83×83. The plot contains 30 contour lines whose levels vary linearly from the minimum to maximum values; and it is in good agreement with that of [46].
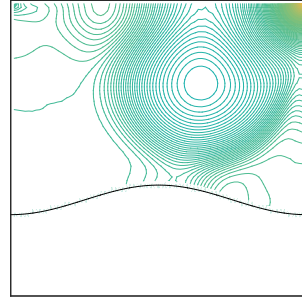
Figure 29: Irregular bottom lid driven cavity, $\beta = 1000$, $Re = 1000$: Static pressure contours of the flow with the grid of 83×83. The plot contains 160 contour lines whose levels vary linearly from the minimum to maximum values.
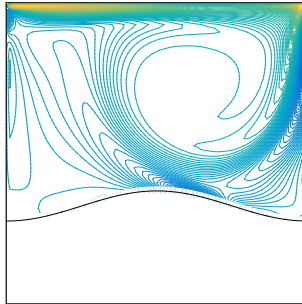

Figure 30: Irregular bottom lid driven cavity, $\beta = 1000$, $Re = 1000$: Iso-vorticity lines of the flow with the grid of 83×83. The plot contains 160 contour lines whose levels vary linearly from the minimum to maximum values.

6. Concluding remarks

The main purpose of this work is to provide a scheme that allows for stable calculation of IRBF approximations at large values of the shape parameter, where the ill-condition problem becomes severe. The increasing flat region of RBF is of particular interest since it often corresponds to the most accurate RBF approximations as shown in recent works [31, 32]. In the paper, we have proposed an idea of using high-order IRBFs to construct combined compact approximations, which allows a more straightforward incorporation of nodal values of first- and second-order derivatives, and yields better accuracy over compact approximations. Then, we have proposed a preconditioning technique to circumvent the ill-condition problems of compact IRBF approaches associated with large values of the shape parameter β and the stability is shown to be significantly improved. In elliptic equation tests, we have found that in the large value range of β the proposed CCIRBF-Precond solutions are many orders of magnitude better than those of the DRBF, CIRBF, and CIRBF-Precond schemes. In the simulation of several fluid flow problems, the new method performs significantly better than the standard central FDM, the HOC and the CIRBF. This study provides an effective tool for the numerical exploration of IRBFs in the large value range of the shape parameter.

Appendix

The following analytic forms of IRBFs are obtained using Mathematica.

$$I_{1i} = \frac{(x - c_i)}{2}A + \frac{a_i^2}{2}B \tag{70}$$

$$I_{2i} = \left(\frac{-a_i^2}{3} + \frac{(x - c_i)^2}{6} \right) A + \frac{a_i^2(x - c_i)}{2}B \tag{71}$$

$$I_{3i} = \left(\frac{-13a_i^2(x - c_i)}{48} + \frac{(x - c_i)^3}{24} \right) A + \left(\frac{-a_i^4}{16} + \frac{a_i^2(x - c_i)^2}{4} \right) B \tag{72}$$

$$I_{4i} = \left(\frac{a_i^4}{45} - \frac{83a_i^2(x - c_i)^2}{720} + \frac{(x - c_i)^4}{120} \right) A + \left(\frac{-3a_i^4(x - c_i)}{48} + \frac{4a_i^2(x - c_i)^3}{48} \right) B \tag{73}$$

where $A = \sqrt{(x - c_i)^2 + a_i^2}$ and $B = ln\left((x - c_i) + \sqrt{(x - c_i)^2 + a_i^2} \right)$.

31

References

[1] R. Hardy, Multiquadric equations of topography and other irregular surfaces, Journal of Geophysical Research 76 (8) (1971) 1905–1915. doi:10.1029/JB076i008p01905.

[2] R. Hardy, Theory and applications of the multiquadric-biharmonic method 20 years of discovery 1968-1988, Computers & Mathematics with Applications 19 (8-9) (1990) 163–208. doi:10.1016/0898-1221(90)90272-L.

[3] M. Buhmann, Multivariate interpolation in odd-dimensional euclidean spaces using multiquadrics, Constructive Approximation 6 (1) (1990) 21–34. doi:10.1007/BF01891407.

[4] W. Madych, S. Nelson, Multivariate interpolation and conditionally positive definite functions.II, Mathematics of Computation 54 (189) (1990) 211–230. doi:10.2307/2008691.

[5] E. Kansa, Multiquadrics-A scattered data approximation scheme with applications to Computational Fluid-Dynamics-I. Surface approximations and partial derivative estimates, Computers & Mathematics with Applications 19 (8–9) (1990) 127–145. doi:10.1016/0898-1221(90)90270-T.

[6] E. Kansa, Multiquadrics-A scattered data approximation scheme with applications to Computational Fluid-Dynamics-II. Solutions to parabolic, hyperbolic and elliptic partial differential equations, Computers & Mathematics with Applications 19 (8–9) (1990) 147–161. doi:10.1016/0898-1221(90)90271-K.

[7] A. Fedoseyev, M. Friedman, E. Kansa, Improved multiquadric method for elliptic partial differential equations via PDE collocation on the boundary, Computers & Mathematics with Applications 43 (3–5) (2002) 439–455. doi:10.1016/S0898-1221(01)00297-8.

[8] T. Driscoll, B. Fornberg, Interpolation in the limit of increasingly flat radial basis functions, Computers & Mathematics with Applications 43 (3–5) (2002) 413–422. doi:10.1016/S0898-1221(01)00295-4.

[9] J. Li, A.-D. Cheng, C. Chen, A comparison of efficiency and error convergence of multiquadric collocation method and finite element method, Engineering Analysis with Boundary Elements 27 (3) (2003) 251–257. doi:10.1016/S0955-7997(02)00081-4.

[10] A.-D. Cheng, M. Golberg, E. Kansa, G. Zammito, Exponential convergence and H-c multiquadric collocation method for partial differential equations, Numerical Methods for Partial Differential Equations 19 (5) (2003) 571–594. doi:10.1002/num.10062.

[11] B. Fornberg, G. Wright, Stable computation of multiquadric interpolants for all values of the shape parameter, Computers & Mathematics with Applications 48 (5–6) (2004) 853–867. doi:10.1016/j.camwa.2003.08.010.

[12] N. Mai-Duy, T. Tran-Cong, Numerical solution of Navier-Stokes equations using multiquadric radial basis function networks, International Journal for Numerical Methods in Fluids 37 (1) (2001) 65–86. doi:10.1002/fld.165.

[13] N. Mai-Duy, T. Tran-Cong, Approximation of function and its derivatives using radial basis function networks, Applied Mathematical Modelling 27 (3) (2003) 197–220. doi:10.1016/S0307-904X(02)00101-4.

[14] N. Mai-Duy, T. Tran-Cong, Numerical solution of differential equations using multiquadric radial basis function networks, Neural Networks 14 (2) (2001) 185–199. doi:10.1016/S0893-6080(00)00095-2.

[15] N. Mai-Duy, T. Tran-Cong, An efficient indirect RBFN-based method for numerical solution of PDEs, Numerical Methods for Partial Differential Equations 21 (4) (2005) 770–790. doi:10.1002/num.20062.

[16] S. Sarra, Integrated multiquadric radial basis function approximation methods, Computers & Mathematics with Applications 51 (8) (2006) 1283–1296. doi:10.1016/j.camwa.2006.04.014.

[17] D. Ngo-Cong, N. Mai-Duy, W. Karunasena, T. Tran-Cong, Local moving least square-one-dimensional integrated radial basis function networks technique for incompressible viscous flows, International Journal for Numerical Methods in Fluids 70 (11) (2012) 1443–1474. doi:10.1002/fld.3640.

[18] C. M. T. Tien, N. Thai-Quang, N. Mai-Duy, C.-D. Tran, T. Tran-Cong, High-order fully coupled scheme based on compact integrated RBF approximation for viscous flows in regular and irregular domains, Computer Modeling in Engineering & Sciences 105 (4) (2015) 301–340. doi:10.3970/cmes.2015.105.301.

[19] C. Tien, N. Thai-Quang, N. Mai-Duy, C.-D. Tran, T. Tran-Cong, A three-point coupled compact integrated RBF scheme for second-order differential problems, Computer Modeling in Engineering & Sciences 104 (6) (2015) 425–469. doi:10.3970/cmes.2015.104.425.

[20] R. Carlson, T. Foley, The parameter R2 in multiquadric interpolation, Computers & Mathematics with Applications 21 (9) (1991) 29–42. doi:10.1016/0898-1221(91)90123-L.

[21] S. Rippa, An algorithm for selecting a good value for the parameter c in radial basis function interpolation, Advances in Computational Mathematics 11 (2-3) (1999) 193–210. doi:10.1023/A:1018975909870.

[22] H. Power, V. Barraco, A comparison analysis between unsymmetric and symmetric radial basis function collocation methods for the numerical solution of partial differential equations, Computers & Mathematics with Applications 43 (3-5) (2002) 551–583. doi:10.1016/S0898-1221(01)00305-4.

[23] C. Shu, H. Ding, K. S. Yeo, Local radial basis function-based differential quadrature method and its application to solve two-dimensional incompressible Navier Stokes equations, Computer Methods in Applied Mechanics & Engineering 192 (7-8) (2003) 941–954. doi:10.1016/S0045-7825(02)00618-7.

[24] E. Larsson, B. Fornberg, Theoretical and computational aspects of multivariate interpolation with increasingly flat radial basis functions, Computers & Mathematics with Applications 49 (1) (2005) 103–130. doi:10.1016/j.camwa.2005.01.010.

[25] E. Kansa, Y. Hon, Circumventing the ill-conditioning problem with multiquadric radial basis functions: Applications to elliptic partial differential equations, Computers & Mathematics with Applications 39 (7–8) (2000) 123–137. doi:10.1016/S0898-1221(00)00071-7.

[26] N. Libre, A. Emdadi, E. Kansa, M. Rahimian, M. Shekarchi, A stabilized RBF collocation scheme for Neumann type boundary value problems, Computer Modeling in Engineering & Sciences 24 (1) (2008) 61–80. doi:10.3970/cmes.2008.024.061.

[27] A. Emdadi, E. Kansa, N. Libre, M. Rahimian, M. Shekarchi, Stable PDE solution methods for large multiquadric shape parameters, Computer Modeling in Engineering & Sciences 25 (1) (2008) 23–41. doi:10.3970/cmes.2008.025.023.

[28] B. Fornberg, E. Larsson, N. Flyer, Stable computations with Gaussian radial basis functions, SIAM Journal on Scientific Computing 33 (2) (2011) 869–892. doi:10.1137/09076756X.

[29] G. Fasshauer, M. Mccourt, Stable evaluation of gaussian radial basis function interpolants, SIAM Journal on Scientific Computing 34 (2) (2012) A737–A762. doi:10.1137/110824784.

[30] D. Stefano, S. Gabriele, A new stable basis for radial basis function interpolation, Journal of Computational & Applied Mathematics 253 (2013) 1–13. doi:10.1016/j.cam.2013.03.048.

[31] E. Larsson, E. Lehto, A. Heryudono, B. Fornberg, Stable computation of differentiation matrices and scattered node stencils based on gaussian radial basis functions, SIAM Journal on Scientific Computing 35 (4) (2013) A2096–A2119. doi:10.1137/120899108.

[32] B. Fornberg, E. Lehto, C. Powell, Stable calculation of Gaussian-based RBF-FD stencils, Computers & Mathematics with Applications 65 (4) (2013) 627–637. doi:10.1016/j.camwa.2012.11.006.

[33] R. Schaback, Error estimates and condition numbers for radial basis function interpolation, Advances in Computational Mathematics 3 (3) (1995) 251–264. doi:10.1007/BF02432002.

[34] C. Franke and R. Schaback, Convergence order estimates of meshless collocation methods using radial basis functions, Advances in Computational Mathematics 8 (4) (1998) 381–399. doi:10.1023/A:1018916902176.

[35] H. Wendland, Computational aspects of radial basis function approximation, Studies in Computational Mathematics 12 (2006) 231–256. doi:10.1016/S1570-579X(06)80010-8.

[36] P. Chu, C. Fan, A three-point sixth-order staggered combined compact difference scheme, Mathematical & computer modelling 32 (3–4) (2000) 323–340. doi:10.1016/S0895-7177(00)00138-2.

[37] N. Thai-Quang, N. Mai-Duy, C.-D. Tran, T. Tran-Cong, High-order alternating direction implicit method based on compact integrated-RBF approximations for unsteady/steady convection-diffusion equations, Computer Modeling in Engineering & Sciences 89 (3) (2012) 189–220. doi:10.3970/cmes.2012.089.189.

[38] N. Mai-Duy, T. Tran-Cong, A compact five-point stencil based on integrated RBFs for 2D second-order differential problems, Journal of Computational Physics 235 (2013) 302–321. doi:10.1016/j.jcp.2012.10.048.

[39] A. J. Wathen, S. Zhu, On spectral distribution of kernel matrices related to radial basis functions, Numerical Algorithms (2015) 1–18doi:10.1007/s11075-015-9970-0.

[40] I. Hassanien, A. Salama, H. Hosham, Fourth-order finite difference method for solving burgers equation, Applied Mathematics & Computation 170 (2) (2005) 781–800. doi:10.1016/j.amc.2004.12.052.

[41] B. Noye, H. Tan, Finite difference methods for solving the two-dimensional advection-diffusion equation, International Journal for Numerical Methods in Fluids 9 (1) (1989) 75–98. doi:10.1002/fld.1650090107.

[42] Y. Ma, C.-P. Sun, D. Haake, B. Churchill, C.-M. Ho, A high-order alternating direction implicit method for the unsteady convection-dominated diffusion problem, International Journal for Numerical Methods in Fluids 70 (6) (2012) 703–712. doi:10.1002/fld.2707.

[43] Z. Tian, X. Liang, P. Yu, A higher order compact finite difference algorithm for solving the incompressible Navier Stokes equations, International Journal for Numerical Methods in Engineering 88 (6) (2011) 511–532. doi:10.1002/nme.3184.

[44] N. Mai-Duy, T. Tran-Cong, A numerical study of 2D integrated RBFNs incorporating Cartesian grids for solving 2D elliptic differential problems, Numerical Methods for Partial Differential Equations 26 (6) (2010) 1443–1462. doi:10.1002/num.20502.

[45] H. Udaykumar, W. Shyy, M. Rao, ELAFINT: A mixed Eulerian-Lagrangian method for fluid flows with complex and moving boundaries, International Journal for Numerical Methods in Fluids 22 (8) (1996) 691–712. doi:10.1002/(SICI)1097-0363(19960430)22:8<691::AID-FLD371>3.0.CO;2-U.

[46] W. Shyy, H. Udaykumar, M. Rao, R. Smith, Computational fluid dynamics with Moving boundaries, Taylor&Francis, 1900 Frost Road, Suite 101, Bristol, PA 19007-1598, 1996.

[47] V. Mariani, A. Prata, A Eulerian-Lagrangian method applied to fluid flow in lid-driven cavities with irregular bottom walls, Numerical Heat Transfer Part B Fundamentals 53 (3) (2008) 206–233. doi:10.1080/10407790701632568.